Extended parity doublet model with a new transport code

Myungkuk Kim,[1,*] Sangyong Jeon,[2] Young-Min Kim,[3] Youngman Kim,[4] and Chang-Hwan Lee[1,†]

[1]*Department of Physics, Pusan National University, Busan 46241, Korea*

[2]*Department of Physics, McGill University, Montreal, Quebec, Canada H3A2T8*

[3]*Department of Physics, Ulsan National Institute of Science and Technology, Ulsan 44919, Korea*

[4]*Rare Isotope Science Project, Institute for Basic Science, Daejeon 34047, Korea*

(Received 25 November 2019; revised manuscript received 21 April 2020; accepted 26 May 2020; published 16 June 2020)

A new transport code "DaeJeon Boltzmann-Uehling-Uhlenbeck" (DJBUU) has been developed and enables us to describe the dynamics of heavy-ion collisions in the low-energy region. To confirm the validity of the new code, we first calculate Au + Au collisions at $E_{\rm beam} = 100A$ and $400A$ MeV and also perform the box calculation to check the detail of collisions and Pauli blocking without using a mean-field potential as suggested by the Transport Code Comparison Project. After confirming the validity of new transport code, we study low-energy heavy-ion collisions by using an extended parity doublet model. Since the distinctive feature of the parity doublet model is the existence of the chiral-invariant mass that contributes to the nucleon mass, we investigate how physical quantities depend on the chiral-invariant mass in heavy-ion collisions at low energies. For this, we calculate physical quantities such as the effective nucleon mass in central collisions and transverse flow in semicentral collisions of Au + Au at $E_{\rm beam} = 400A$ MeV with different values of the chiral-invariant masses.

DOI: 10.1103/PhysRevC.101.064614

I. INTRODUCTION

Understanding asymmetric nuclear matter is one of the key issues in contemporary nuclear physics. The study of exotic nuclei, compact stars, core-collapsed supernovae and many facets of the QCD phase diagram all critically depend on such understanding. Forthcoming facilities [1] such as Rare isotope Accelerator complex for ON-line experiments (RAON), the Facility for Rare Isotope Beams (FRIB), the GSI Facility for Antiproton and Ion Research (FAIR), and the Radioactive Isotope Beam Factory (RIBF) at RIKEN will be creating highly asymmetric nuclear matter by colliding heavy ions for the goal of understanding neutron-rich matter.

Heavy-ion collisions (HICs) offer a great opportunity to research a wide range of densities, temperatures, and isospin asymmetries. However, some important quantities in dense-matter studies such as the nuclear symmetry energy and its slope parameter are not directly accessible in such experiments. An important way to extract such information from the HICs is to use nuclear transport simulations to test out various scenarios. The purpose of this work is to study asymmetric nuclear matter using the Boltzmann-Uehling-Uhlenbeck (BUU) approach.

Transport theories have been applied to heavy-ion collision simulations since the 1980s [2–4]. Currently, two types of transport approaches are in wide use. One is the BUU approach, which evolves the one-particle phase density by propagating test particles in the mean fields between collisions. The other is the quantum molecular dynamics (QMD) approach, which attempts to evolve particles according to the given many-body Hamiltonian. To understand and reduce the uncertainty between different codes, a few transport code comparison projects have been carried out over the years [5–8]. In this work, we first compare our results with those in Refs. [6,7] in Sec. III to ensure that our BUU model is performing within the established norm before applying it to the extended parity doublet model in Sec. IV.

There are several existing BUU codes developed for heavy-ion collisions, such as GIBUU [9–11], IBUU [12–15], and RBUU [16–18]. In this paper, we use the newly developed DJBUU (DaeJeon Boltzmann-Uehling-Uhlenbeck) code. This code is optimized, for the moment, to HICs up to a few hundred A MeV.

As an application of DJBUU in heavy-ion collisions, we study the extended parity doublet model in this work. The parity doublet model was formulated in Refs. [19,20] and applied to the dense matter in Refs. [21–31]. As is well known, the mass of current quarks can explain only about 2% of the nucleon mass and the rest may be explained by other effects such as spontaneous chiral symmetry breaking. In the parity doublet model, the nucleon mass has a contribution from the chiral-invariant mass, apart from the contribution from spontaneous chiral symmetry breaking. At present, the origin of the chiral-invariant mass is not well understood and its value is yet uncertain.

Since the chiral symmetry is expected to be partially restored in dense matter, change of the nucleon mass, caused by the reduction in the chiral condensate, results in the change

*myung.k.kim@pusan.ac.kr

†clee@pusan.ac.kr

of observables in HICs. Therefore, in order to constrain the value of the chiral-invariant mass in the parity doublet model, it is important to investigate the effect of the partial chiral symmetry restoration in low-energy heavy-ion collisions. In Ref. [22], the chiral-invariant mass was estimated to be $m_0 \approx 800$ MeV by using nuclear matter properties, especially incompressibility. In an extended parity doublet model [28], the properties of nuclear matter were reproduced reasonably well with the chiral-invariant mass in the range from 500 to 900 MeV. In this work, we implement the extended parity doublet model [28,32] in the DJBUU code and simulate heavy-ion collisions with various values of the chiral-invariant mass in an effort to better understand its value.

In Sec. II, we introduce the newly developed transport code DJBUU, including basic equations and numerical schemes. In Sec. III, we compare our results with DJBUU in both HICs and box calculations with those of the Transport Code Comparison Project (TCCP) [6]. In Sec. IV, we summarize the basic formalism of the extended parity doublet model implemented in the new transport code and parameter sets extracted from the nuclear structure calculation with the parity doublet model. In Sec. V, we present our results of the time evolution of mass splitting and anisotropic transverse flow with various values of the chiral-invariant mass. In Sec. VI, final conclusion and discussion are summarized.

II. DESCRIPTION OF DAEJEON BOLTZMANN-UEHLING-UHLENBECK CODE

In this section, we introduce the recently developed transport code DJBUU. The relativistic BUU equation with a mean-field potential is given by

$$\left[p^\mu \partial^x_\mu - \left(p_\mu F^{\mu\nu} - m_i^* \partial^\nu_x m_i^*\right)\partial^p_\nu\right]\frac{f_i(\mathbf{x},\mathbf{p};t)}{E} = \mathcal{C}^i_{\rm coll}, \quad (1)$$

where $f_i(\mathbf{x},\mathbf{p};t)$ is the phase-space density of hadron species i, $F^{\mu\nu} \equiv \partial^\mu V^\nu - \partial^\nu V^\mu$ is the field-strength tensor associated with the vector-meson mean field V^μ, and m_i^* is the effective mass of the ith hadron species that includes the effect of the space-time dependent chiral condensate. The superscript x and p on the partial derivatives indicate the spatial (x) and the momentum (p) derivatives. All possible collision processes including hadron i and other hadron species j are described by the collision term $\mathcal{C}^i_{\rm coll}$. For example, the elastic collision between two baryon species i and j is described by

$$\begin{aligned} C_{ij} = \frac{1}{2}\int \frac{d^3p_1'}{(2\pi)^3 2E_{p_1'}} \int \frac{d^3p_2}{(2\pi)^3 2E_{p_2}} \int \frac{d^3p_2'}{(2\pi)^3 2E_{p_2'}} \\ \times |\mathcal{M}_{ij}|^2 (2\pi)^4 \delta(p_1 + p_2 - p_1' - p_2') \\ \times [f_i(\mathbf{p}_1') f_j(\mathbf{p}_2') \{1 - f_i(\mathbf{p}_1)\}\{1 - f_j(\mathbf{p}_2)\} \\ - f_i(\mathbf{p}_1) f_j(\mathbf{p}_2) \{1 - f_i(\mathbf{p}_1')\}\{1 - f_j(\mathbf{p}_2')\}]. \end{aligned} \quad (2)$$

where we suppressed the common t and $\mathbf{x}$ dependence in the phase-space densities for the sake of brevity. The first term in Eq. (2) describes the collision process in which the energy level defined by the momentum $\mathbf{p}_1$ gains a particle, and the second term in Eq. (2) describes the collision process in which the energy-level defined by the momentum $\mathbf{p}_1$ loses a particle. The $(1 - f)$ factors associated with the final-state particles implement Pauli blocking. The scattering matrix element $\mathcal{M}_{ij}$ we use is the tree-level in-vacuum matrix elements.

To solve for the phase-space density, $f_i(\mathbf{x},\mathbf{p};t)$, we use test particle method which was first introduced to HIC simulations by Wong [34] in the early 1980s. In this method, each physical particle is split into $N_{\rm test}$ test particles. Hence, the phase space $\hat{f}_i$ and the cross section $\hat{\sigma}_{1,2\to 1',2'\ldots N'}$ used in the simulation are scaled as

$$\hat{f}_i(\mathbf{x},\mathbf{p};t) = f_i(\mathbf{x},\mathbf{p};t)/N_{\rm test}, \quad (3)$$

$$\hat{\sigma}_{1,2\to 1',2'\ldots N'} = \sigma_{1,2\to 1',2'\ldots N'}/N_{\rm test}, \quad (4)$$

where $f_i(\mathbf{x},\mathbf{p};t)$ and $\sigma_{1,2\to 1',2'\ldots N'}$ are the physical phase-space density and the cross section, respectively. In this work, we take 100 test particles for each nucleon ($N_{\rm test} = 100$) and perform ten independent simulations. The simulated phase-space density is represented by

$$\hat{f}_i(\mathbf{x},\mathbf{p};t) = \frac{(2\pi)^3}{N_{\rm test}} \sum_{\alpha=1}^{N} g_x(\mathbf{x} - \mathbf{x}_\alpha(t)) g_p(\mathbf{p} - \mathbf{p}_\alpha(t)), \quad (5)$$

where N is the total number of test particles and $\mathbf{x}_\alpha$ and $\mathbf{p}_\alpha$ are the coordinate and momentum of the αth test particle, respectively. The functions g_x and g_p are the profile functions in the coordinate and momentum spaces. In DJBUU, the following polynomial function is used for the profile instead of the often-used Gaussian function:

$$g(\mathbf{u}) = g(u) = \mathcal{N}_{m,n}[1 - (u/a_{\rm cut})^m]^n \text{ for } 0 < u/a_{\rm cut} < 1. \quad (6)$$

This profile function has some advantages, such as exact integrability and smoothness near the finite endpoint at $a_{\rm cut}$. In this work, $m = 2$ and $n = 3$ are used.

In DJBUU, the dense-medium effects are described by the mean fields obtained from the relativistic Lagrangian density consisting of nucleons, isoscalar (Lorentz scalar σ, Lorentz vector ω), and isovector (Lorentz vector ρ) mesons:

$$\begin{aligned} \mathcal{L} = \bar{\psi}\Big[& i\gamma_\mu \partial^\mu - (m_N + g_\sigma \sigma) - g_\omega \gamma_\mu \omega^\mu \\ & - g_\rho \gamma^\mu \vec{\tau}\cdot\vec{\rho}^{\,\mu} - \frac{e}{2}\gamma_\mu(1+\tau^3)A^\mu\Big]\psi \\ & + \frac{1}{2}\left(\partial_\mu\sigma\,\partial^\mu\sigma - m_\sigma^2\sigma^2\right) - \frac{1}{3}a\sigma^3 - \frac{1}{4}b\sigma^4 \\ & + \frac{1}{2}m_\omega^2\omega_\mu\omega^\mu + \frac{1}{2}m_\rho^2\vec{\rho}_\mu\cdot\vec{\rho}^{\,\mu} \\ & - \frac{1}{4}\Omega_{\mu\nu}\Omega^{\mu\nu} - \frac{1}{4}\vec{R}_{\mu\nu}\cdot\vec{R}^{\mu\nu} - \frac{1}{4}F_{\mu\nu}F^{\mu\nu}, \end{aligned} \quad (7)$$

where the over-arrow on $\vec{\rho}$ indicates the isospin vector nature of ρ mesons and field-strength tensors for the vector mesons (ω and ρ) and the electromagnetic field (A_μ) are defined as

$$\Omega_{\mu\nu} = \partial_\mu\omega_\nu - \partial_\nu\omega_\mu, \quad (8)$$

$$\vec{R}_{\mu\nu} = \partial_\mu\vec{\rho}_\mu - \partial_\nu\vec{\rho}_\nu, \quad (9)$$

$$F_{\mu\nu} = \partial_\mu A_\nu - \partial_\nu A_\mu. \quad (10)$$

TABLE I. Mean-field parameter set and vacuum masses of all mesons in DJBUU taken from Ref. [33]. Coupling constants of mesons are defined as $f_i \equiv (g_i^2/m_i^2)$, $i = \sigma,\ \omega,\ \rho$, and σ self-interaction terms are $A \equiv a/g_\sigma^3$ and $B \equiv b/g_\sigma^4$. All the dimensions of masses are in GeV.

Parameter	f_σ (fm^2)	f_ω (fm^2)	f_ρ (fm^2)	A (fm^{-1})	B	m_N	m_σ	m_ω	m_ρ
	10.33	5.42	0.95	0.033	−0.0048	0.938	0.5082	0.783	0.763

In the relativistic mean-field approximation, a test particle propagates according to the classical equations of motion

$$\frac{d\mathbf{x}_\alpha}{dt} = \frac{\mathbf{p}_\alpha}{E_\alpha},$$
$$\frac{d\mathbf{p}_\alpha}{dt} = -\nabla V_\alpha^0 - \frac{m_\alpha^* \nabla m_\alpha^*}{E_\alpha}. \tag{11}$$

Here, α is the particle label, $E_\alpha = (\mathbf{p}_\alpha^2 + m_\alpha^{*2})^{1/2}$ is the energy, V_α^0 is the vector potential composed of ω and ρ^0 vector-meson mean fields, and m_α^* is the effective mass in a dense medium. For the nucleons, the effective mass is given by $m_N^* = m_N - g_\sigma \sigma$ where σ is the sigma meson mean field and g_σ is the coupling constant. A more detailed code description can be found in Ref. [35]. For the comparison with the TCCP results, we are taking a particular parameter set (Set I) from Ref. [33], as suggested by the TCCP. The mean-field parameters and vacuum masses of nucleons and mesons are summarized in Table I. Following the TCCP procedures detailed in Ref. [6], we neglect the derivatives when solving the mean-field equations and only the time component of the vector-meson fields are used.

At each time step, particles are sampled and paired with other test particles which are geometrically closer than $d \leqslant \sqrt{\hat{\sigma}/\pi}$. In DJBUU, particles which have undergone scatterings are not allowed to decay in the same time step, and they are not allowed to scatter further until they are sufficiently separated from their scattering partners. Uncertainties caused by these constraints can be reduced by taking smaller time steps.

III. COMPARISON WITH TRANSPORT CODE COMPARISON PROJECT

Many transport codes of BUU and QMD type have been developed for heavy-ion collisions. The main purpose of the Transport Code Comparison Project (TCCP) is to have better predictions of the important physical quantities of HICs by reducing simulation uncertainties among different codes. The main goal of this section is to validate DJBUU by comparing its results with the TCCP results.

The project has already published results for Au + Au collisions, box calculations for collisions and box calculation for pion production [6–8]. Ideally, all codes should give the same results starting from the same initial configuration. However, the TCCP found that the numerical uncertainties among different codes reach up to 30%. Because of the large uncertainties, the TCCP published other papers focused on collisions and Pauli blocking and pion production [7,8]. They are also preparing a paper for the mean-field dynamics in the box calculation [36]. Even though there are differences among the codes, the results from the project can be used to test the validity of the newly developed DJBUU code. All the results below were obtained by following the TCCP procedures and options, which are briefly described below.

For the heavy-ion collisions (^{197}Au + ^{197}Au), we consider two different beam energies, $E_{\rm beam} = 100A$ MeV (the B mode in Ref. [6]) and $400A$ MeV (the D mode in Ref. [6]). We use the same initial conditions as in the TCCP, including the impact parameter fixed at $b = 7$ fm. We also consider the same three modes studied in TCCP: (i) only the mean fields are turned on without collisions (Vlasov), (ii) only collisions are turned on without the mean fields (Cascade), and (iii) both the mean fields and the collisions are turned on (Full). Only elastic collisions of nucleons are considered. The included mean fields are σ, ω, and ρ^0. For comparison with the TCCP, we focus on initialization, propagation, collision, and final distribution.

For the infinite-matter calculation (box calculation), we set the box size to be 20 fm and randomly distribute nucleons to make the average density be the nuclear saturation density (680 protons and 680 neutrons in a cube with 20 fm edges). In the momentum space, particle momenta are randomly distributed in the corresponding Fermi sphere for two temperatures: $T = 0$ MeV and $T = 5$ MeV. Only the collision and Pauli blocking effects without the mean fields are considered in the box calculation. Again, only elastic collisions of nucleons are considered and the protons and the neutrons have equal vacuum mass. All results shown below are calculated with 100 test particles and averaged over ten independent runs.

A. Heavy-ion collisions

In this section, we compare our results with those of the TCCP on the time evolution of density distributions, collision rates, Pauli blocking factors, and momentum distributions.

One of the most important features that has to be checked in the transport simulation is the stability of nuclei. Once a nucleus is generated, it should not collapse nor disperse away unless it experiences a collision with another nucleus. Figure 1 shows the time evolution of the averaged density profile of a stationary gold nucleus. In the TCCP, the Woods-Saxon form is used for the initial configuration of nuclei. However, in our simulation, we use relativistic Thomas-Fermi form because it is more consistent with the mean-field dynamics. The simulation has been performed with an extremely large impact parameter $b = 20$ fm so that the two nuclei will not collide. Our results in Fig. 1 show that the density distributions of nuclei are oscillating. However, even though the initial configuration is different, we confirm that the stability of stationary nuclei in the DJBUU code is within the uncertainty of the transport model comparison project.

For the processes with collisions, we take the impact parameter $b = 7$ fm for Au + Au collisions. Figure 2 shows

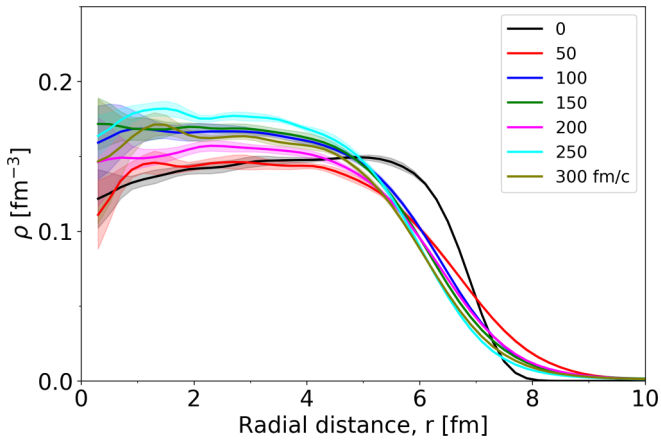

FIG. 1. Time evolution of the Au density profile in the intervals of 50 fm/c at an incident energy of 100A MeV. This is the average density of both projectile and Au target. Statistical uncertainty is shown as a band around the mean.

the evolution of nuclear density in a typical collision. In the figure, we show the density contours in the x-z plane at 20 fm/c time intervals in Au + Au collisions with incident energy at 100A MeV. Here, x is the direction of the impact parameter and z is the beam direction. In this particular example, Coulomb interaction is not included and only elastic NN scatterings are included. Maximum density above $1.5\rho_0$ is reached near $t = 20$ fm/c, and the sideward flows are developed during $t = 40$–80 fm/c, which is consistent with the results of the TCCP study.

Following the TCCP procedure, we now check the successful collision rates and the Pauli blocking effects as a function of total energy in the center-of-mass frame for each collision. Even though these quantities are not directly detectable in experiments, they are worth a close look to check the validity of the code. In Fig. 3, the number of total and successful collisions are shown in the upper panel, and the Pauli blocking factors, defined as the fraction of aborted collisions, are shown in the lower panel. All quantities in the figure are integrated over the whole evolution time, and only cascade and full

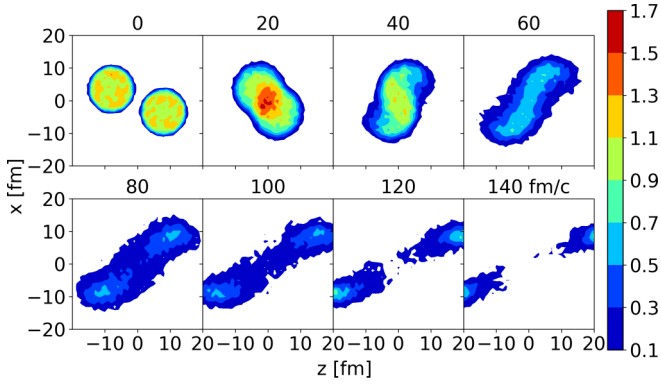

FIG. 2. Time evolution of density contours in Au + Au collision with an impact parameter $b = 7$ fm and incident-beam energy of 100A MeV. Numbers on the top of each plot represent time in units of fm/c.

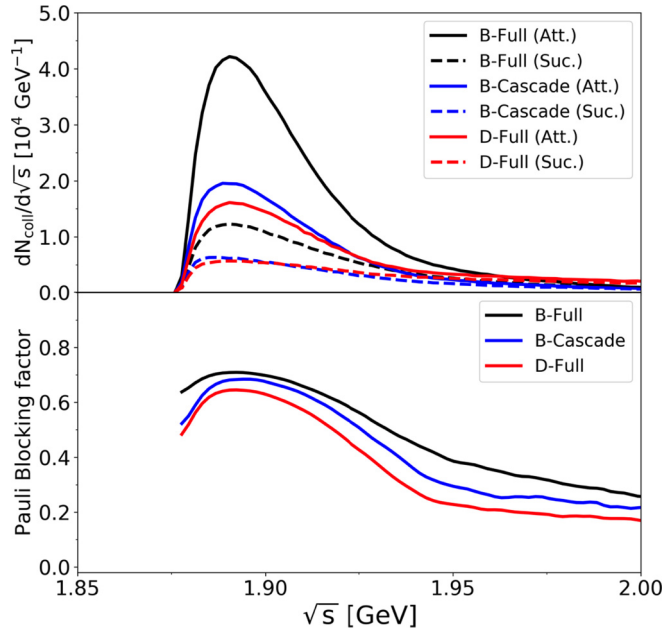

FIG. 3. Number of attempted and successful collisions (upper panel) and Pauli blocking factor in Au + Au collisions (lower panel) for two different incident energies: 100A MeV (B) and 400A MeV (D).

mode simulations are plotted since collisions do not occur in the Vlasov mode. Even though the effective mass has to be used for the total energy in the center-of-mass frame, $\sqrt{s} = 2(m_N^{*\,2} + p^2)^{1/2}$, vacuum mass is used for $\sqrt{s}$ in this plot to compare with other results of the transport code comparison project [6].

In the figure, it is clearly seen that the collision number distribution has a peak at $\sqrt{s} = 1.89$ GeV for $E_{\rm beam} =$ 100A MeV (B mode), which is slightly above the two-nucleon threshold energy. The peak is slightly shifted to a higher value for $E_{\rm beam} = 400A$ MeV (D mode) because there are more nucleons with higher momentum. The full mode with the mean fields at low energy (B Full) has more collisions than those the B-Cascade mode without the mean fields, or the D-Full mode with higher incident energy. This indicates that the mean-field facilitates collisions and the slightly lower number of collisions for the D mode reflects the fact that the total cross section is a decreasing function of $\sqrt{s}$ in this energy region. The blocking factor is largest near the peak of the number of collisions because the phase-space volumes of the occupied nuclei are largest at the peak energy. The TCCP results for the collision numbers and the Pauli blocking factor varies quite significantly (see Figs. 7 and 8 in Ref. [6]). Our results are all well within the variation.

Having checked the overall collision dynamics, we now move on to observable results. In heavy-ion collisions, the final-state momentum distribution encodes a lot of information on the bulk evolution. In the transverse plane, the anisotropic collective flow in the impact-parameter direction reflects how the original energy flow in the beam direction translates into the transverse pressure due to interactions. In the longitudinal (beam) direction, the shape of the rapidity

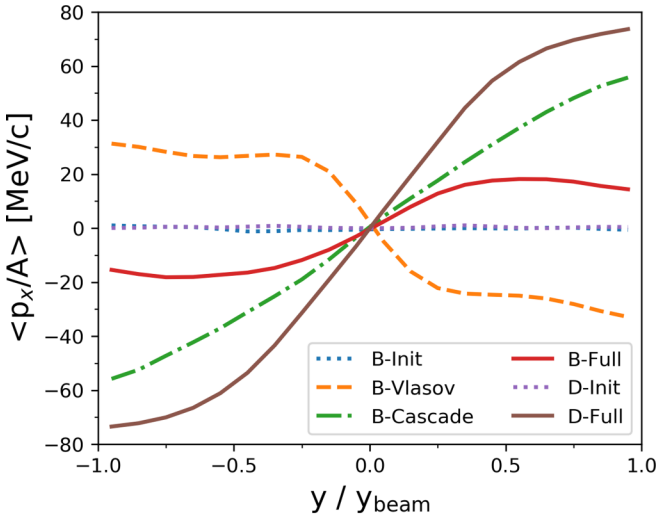

(a) Transverse flow

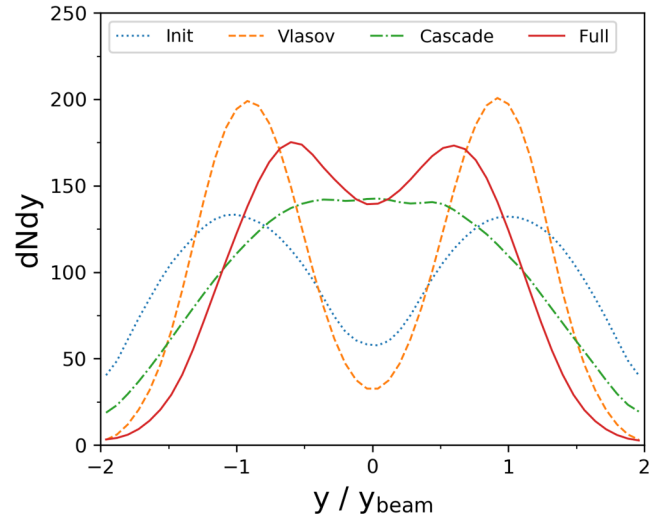

(b) Rapidity distribution in B mode

FIG. 4. The particle distribution in impact parameter (x) and beam direction with respect to the reduced rapidity. (a) Initial and final transverse flow for three different modes (Vlasov, Cascade, and Full) with two different beam energies (B: 100A MeV and D: 400A MeV). (b) Initial and final rapidity distributions with $E_{\rm beam} =$ 100A MeV (B). Here, the impact parameter $b = 7$ fm.

distribution reflects how the longitudinal momentum transforms into transverse pressure.

To compare with results from other codes, we generated events using the same initial conditions as in Ref. [6]. The average momentum in the x direction at different rapidities are shown in Fig. 4(a). This particular observable is sensitive to the interaction between the spectator nucleons and the participant nucleons. As it should be, the initial momentum distribution is almost uniform in the x directions for both the 100 MeV beam energy (B-init) and the 400 MeV beam energy (D-init). However, the final momentum distributions are strongly influenced by the presence of the mean fields and scatterings. If the scatterings are turned off, then higher

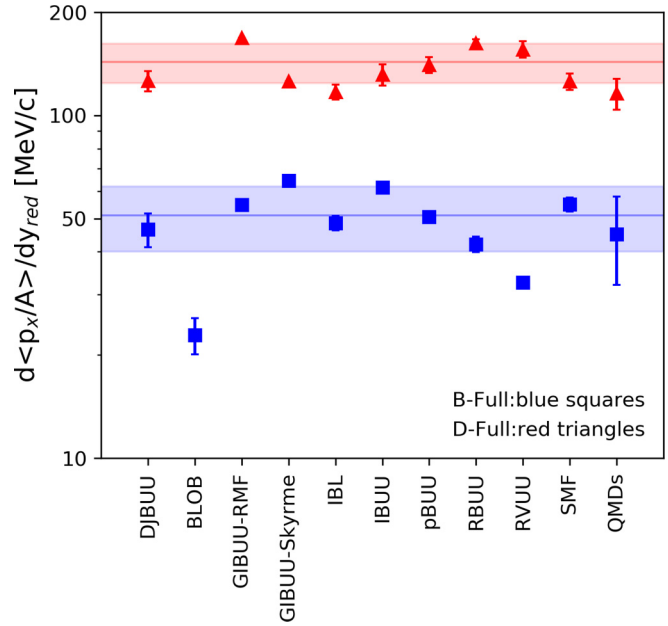

FIG. 5. Slope parameters of DJBUU, nine BUUs, and QMDs at midrapidity. The two shaded regions are the mean and standard deviation of the nine BUUs at beam energy 100A MeV (blue) and 400A MeV (red).

baryon density generates higher σ mean field, which provides more attraction towards the spectator nucleons. On the other hand, if the mean fields are turned off, then higher baryon density implies higher rates of scatterings between the spectators and the participants which provides effective pressure away from the spectators. This effect is most clearly seen in the low-energy collisions at $E_{\rm beam} = 100A$ MeV because the spectators are slower to move away from the collision region. One can see that the Vlasov mode (B-Vlasov) and the Cascade mode (B-Cascade) clearly exhibit slopes of opposite sign. In the full mode (B-Full), the effect of scattering is larger than that of the mean fields, causing a positive but more gentle slope at the midrapidity region. At $E_{\rm beam} = 400A$ MeV, the scattering effect is even stronger. We note that the attraction caused by scalar mean fields and the repulsion caused by vector mean fields balance at $E_{\rm crit}$ ($\approx$140A MeV in Ref. [37]), and the mean-field effect is attractive for $E_{\rm beam} < E_{\rm crit}$ but repulsive for $E_{\rm beam} > E_{\rm crit}$.

In Fig. 4(b), the rapidity distributions with $E_{\rm beam} =$ 100A MeV (B-mode) are summarized. Initially, the projectile and target sit at the reduced rapidity $y/y_{\rm beam} = \pm 1$. Positive (negative) rapidity corresponds to the projectile (target). The peaks in the final distribution of Vlasov mode are shifted toward the center because of the attractive effect in B-Vlasov model. Without the mean fields (B-Cascade mode), the distribution fills the midrapidity region because of the stopping. In the B-Full mode where both mean-field and collision effects are considered, the final distribution is between those of B-Vlasov and B-Cascade. These results are all consistent with those presented in the TCCP study.

Figure 5 compares the slope parameter which is a linear fit of transverse flow in the rapidity range $|y/y_{\rm beam}| < 0.38$.

TABLE II. Pauli blocking factor at $\sqrt{s} = 1.9$ GeV, and the mean transverse flow of DJBUU, BUUs, and QMDs at B-Cascade or Full (100A MeV with only collisions or both collisions and the mean field) and D-Full (400A MeV). The mean flow of BUUs and QMDs are from Ref. [6].

	Pauli blocking			Slope parameter		[MeV/c]
	DJBUU	BUU	QMD	DJBUU	BUU	QMD
B-Cascade	0.677	0.65 ± 0.129	0.51 ± 0.212			
B-Full	0.700	0.75 ± 0.124	0.70 ± 0.136	46.5 ± 5.3	51 ± 11	45 ± 13
D-Full	0.630	0.63 ± 0.145	0.55 ± 0.138	126.1 ± 8.7	143 ± 19	116 ± 12

In the TCCP study, the mean and standard deviation of slope parameter was 51 ± 11 MeV/c at 100A MeV and 143 ± 19 MeV/c at 400A MeV among the nine participating BUU codes. The QMDs had 45 ± 13 MeV/c at 100A MeV and 116 ± 12 MeV/c at 400A MeV.

For the D-Full mode, the DJBUU result (126.1 ± 8.7 MeV/c) is somewhat lower than that of other relativistic BUU codes (GIBUU-RMF, RBUU, and RVUU). For the B-Full mode, the DJBUU result (46.5 ± 5.3 MeV/c) is consistent with others. This could be due to the differences in the mean-field calculations among the relativistic codes. Unfortunately, those differences were not extensively explored in previous studies. Nevertheless, our results are all within the uncertainties of the overall TCCP values.

The comparison results are summarized in Table II. In summary, the DJBUU results are consistent with those in the TCCP within the model uncertainties.

B. Infinite dense matter

Because of the differences in the implementation of the transport simulations for HICs, the TCCP suggested box calculations for checking three important ingredients in the transport code: collisions and Pauli blockings, mean-field dynamics, and pion production Ref. [7]. In this work, for the low-temperature simulations, we focus on the collisions and blockings because pion production is negligible at low temperature. In this section, we compare our results with those in the second TCCP paper Ref. [7].

For the box calculation, Ref. [7] suggested two collision modes (C, CB) for two temperatures (T0, T5), and two Pauli blocking options (OP1, OP2) for CB. Here, the mode C is a cascade mode without the mean fields and the Pauli blocking, and the mode CB is a cascade mode without the mean fields. T0 and T5 correspond to $T = 0$ MeV and $T = 5$ MeV, respectively. The option OP1 is with the collision and blocking methods intrinsic to DJBUU, as explained in Sec. II. The option OP2 is with the reference criteria for both collisions and blocking provided by the TCCP for comparison in which the Pauli blocking is always calculated with the initial thermal distribution regardless of the local environment of the particle at the given time. In total, six sets of calculations are carried out, as suggested by the TCCP; they are denoted CT0, CT5, CBOP1T0, CBOP1T5, CBOP2T0, and CBOP2T5.

In Figs. 6(a) and 6(b) we show the momentum distributions at $t = 0$, 20, 60, 100, and 140 fm/c with $T = 0$ (T0) and 5 MeV (T5), respectively. Even though initial momenta of particles are distributed according to the Fermi-Dirac distributions for both temperatures, the final distributions of the momentum are expected to follow the classical Boltzmann distributions due to the diffusion intrinsic to the coarse-graining procedure to calculate the phase densities [6,38]. This numerical artifact was also observed in other models. In our simulation, the fitted temperatures of the final distributions, with the assumption of the relativistic Boltzmann distribution, are $T_B = 14.355$ and 15.399 MeV for T0 and

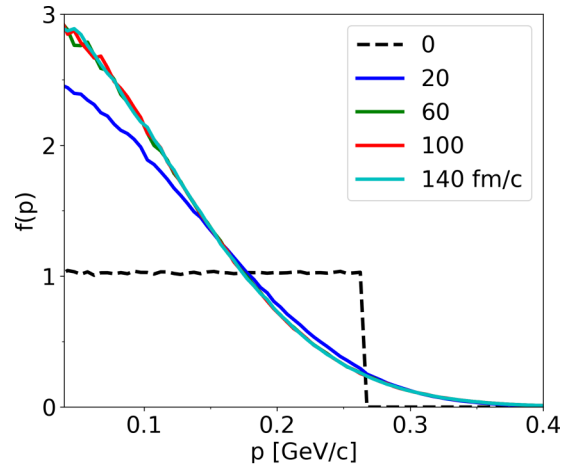

(a) CT0

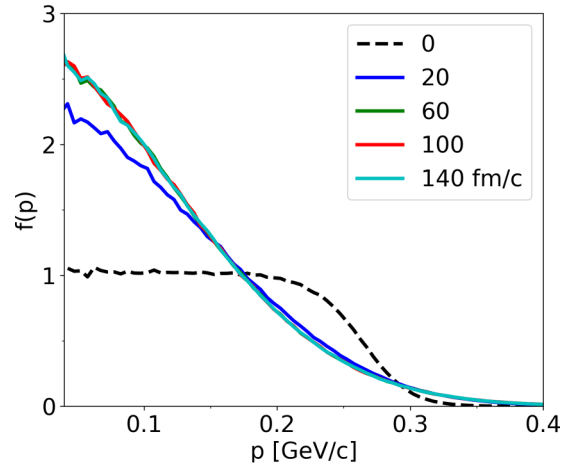

(b) CT5

FIG. 6. Momentum distributions at time $t = 0$, 20, 60, 100, and 140 fm/c for the cascade mode C (without Pauli blocking) with (a) $T = 0$ MeV and (b) 5 MeV.

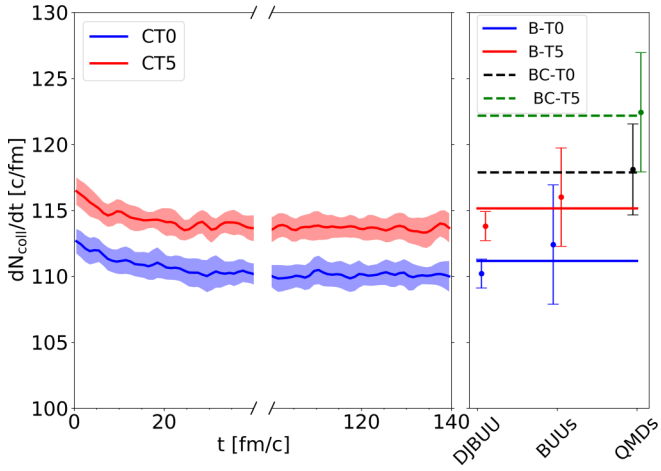

FIG. 7. (left) Time evolution of collision rate $dN_{\rm coll}/dt$ without Pauli blocking at $T = 0$ (CT0) and 5 MeV (CT5). (right) Averaged collision rate with time interval from 60 to 140 fm/c for DJBUU, BUUs, and QMDs. The straight solid and dashed lines represent the reference values from relativistic Boltzmann at $T = 0$ (B-T0) and 5 MeV (B-T5) and relativistic basic cascade code results at $T = 0$ (BC-T0) and 5 MeV (BC-T5).

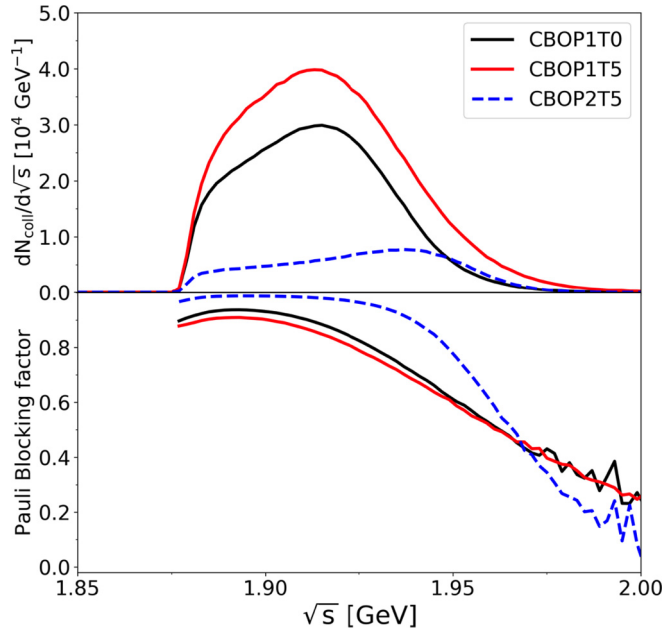

FIG. 8. (upper panel) Successful collision rate as a function of the center-of-mass energy for $T = 0$ (CBOP1T0) and 5 MeV (CBOP1T5). (lower panel) Center-of-mass energy distribution of averaged Pauli blocking factors defined as $1 - \frac{\text{successful collisions}}{\text{attempted collisions}}$.

T5, respectively. These values are very close to the values obtained in the TCCP: $T_B = 14.284$ and 15.364 MeV for T0 and T5, respectively [7].

Figure 7 shows the time evolution of the collision rate, $dN_{\rm coll}/dt$, for the mode C (without Pauli blocking) with 1σ uncertainties. The initial collision rates are 112.8 and 116.8 for $T = 0$ and 5 MeV, respectively. One can compare these values with the reference values in the TCCP [7]: 114.0 or 115.2 for $T = 0$ and 117.8 or 119.0 for $T = 5$ MeV. Note that they obtained two reference values for each temperature by changing the time step: with and without the time dilation factor. Around $t = 40$ fm/c in Fig. 6, the momentum distributions become Boltzmann likely distributions. Hence, after $t = 40$ fm/c, we expect that the system reaches equilibrium and the collision rates saturate. In our simulation, the saturated collision rates averaged over time from 60 to 140 fm/c are 110.2 and 113.8 for T0 and T5, respectively.

The right panel of Fig. 7 shows collision rates of DJBUU and other transport codes (BUUs and QMDs). The horizontal lines are the reference values for two temperatures $T = 0$ and 5 MeV. The reference values labeled with B come from evaluating the equilibrium collision rates using Boltzmann distributions. The reference values labeled with BC come from calculating the collision rates in the "basic cascade" simulations in which only the collision pairs at each time step are counted without actually colliding them. Most BUU types including DJBUU are close to the value of the relativistic Boltzmann calculation while most of QMDs are close to the relativistic basic cascade.

The successful collision rate and Pauli blocking factor in DJBUU (OP1) are shown in Fig. 8. The successful collisions are peaked around 1.92 GeV while the attempted collisions are peaked at slightly lower energy (not on the figure). The time-averaged Pauli blocking factor as a function of energy is plotted in the lower panel. Again, the TCCP study found that these results vary quite substantially between the tested codes, just as they were in the Au+Au collision study. The DJBUU results are certainly within the variation shown in Fig. 5 of Ref. [7]. The dashed line in the figure corresponds to the OP2, in which the Pauli blocking is always calculated with the initial Fermi-Dirac distribution with $T = 5$ MeV.

In Table III, we summarize the successful collision rates in box calculations with Pauli blocking for initial temperatures at $T = 0$ and 5 MeV. We checked the collision rates for the first time step (first Δt) and the rate averaged over time interval 60–140 fm/c as in the TCCP. In the comparison project, most QMD families have large collision rates, 20–40 c/fm, but BUU types have smaller rates, 10–20 c/fm except for pBUU. The collision rates of DJBUU (CBOP1) are consistent with the BUU types. This assures that the collisions and blockings are working properly in DJBUU. With the ideal Pauli blocking option at $T = 0$ (CBOP2T0), collision rates are zero since all

TABLE III. Successful collision rates $dN^{\rm suc}_{\rm coll}/dt$ with Pauli blocking for four options in the unit of c/fm. The row marked with "First Δt" has the rate for the first time step, while the row marked with $t_{\rm avg}$ has the rate averaged over the time interval 60–140 fm/c. The minimum and maximum collision rates are taken from Fig. 8 of Ref. [7].

	DJBUU		BUU	QMD
	OP1T0	OP1T5	OP1T5	OP1T5
First Δt	11.217	16.372	4.2–23.12	3.34–38.83
$t_{\rm avg}$	11.161	16.077	4.2–22.67	3.34–40.91

collisions must be blocked. This is because in OP2 at $T = 0$ the Fermi-Dirac distribution is either 1 or 0. For the ideal option at $T = 5$ MeV (CBOP2T5), collisions rates are slightly lower than the theoretical estimate by the TCCP, 3.5 c/fm (relativistic cases), but acceptable.

In this section, we have compared our results for collisions and blocking with the TCCP results. We have also tested other physical quantities, such as the pion production suggested by the project and found that our results are consistent other results. We can conclude that DJBUU has successfully passed the infinite matter test.

IV. THE EXTENDED PARITY DOUBLET MODEL

Up to now, we have applied our model to the idealized cases to test the inner workings of the code. With the confidence gained by testing DJBUU against the TCCP tests, we now apply DJBUU to realistic heavy-ion collisions and test a specific physics model. The physics model we choose to test is the extended parity doublet model (EPDM) [28]. The motivation for implementing this model in DJBUU is to see how the observable from HICs depends on the chiral-invariant mass. In this section, we briefly introduce the extended parity doublet model.

The Lagrangian for the EPDM constructed in Ref. [28] is given by

$$\begin{aligned}\mathcal{L} = {} & \bar{\psi}_1 i\gamma_\mu \partial^\mu \psi_1 + \bar{\psi}_2 i\gamma_\mu \partial^\mu \psi_2 + m_0(\bar{\psi}_2\gamma_5\psi_1 - \bar{\psi}_1\gamma_5\psi_2) \\ & + g_1\bar{\psi}_1(\sigma + i\gamma_5\vec{\tau}\cdot\vec{\pi})\psi_1 + g_2\bar{\psi}_2(\sigma - i\gamma_5\vec{\tau}\cdot\vec{\pi})\psi_2 \\ & - g_{\omega NN}\bar{\psi}_1\gamma_\mu\omega^\mu\psi_1 - g_{\omega NN}\bar{\psi}_2\gamma_\mu\omega^\mu\psi_2 \\ & - g_{\rho NN}\bar{\psi}_1\gamma_\mu\vec{\rho}^{\,\mu}\cdot\vec{\tau}\psi_1 - g_{\rho NN}\bar{\psi}_2\gamma_\mu\vec{\rho}^{\,\mu}\cdot\vec{\tau}\psi_2 \\ & - e\bar{\psi}_1\gamma^\mu A_\mu\frac{1-\tau_3}{2}\psi_1 - e\bar{\psi}_2\gamma^\mu A_\mu\frac{1-\tau_3}{2}\psi_2 + \mathcal{L}_M,\end{aligned} \tag{12}$$

where the right-handed and the left-handed components of the baryon fields ψ_1 and ψ_2 transform as

$$\begin{aligned}\psi_{1R} \to R\psi_{1R}, \quad \psi_{1L} \to L\psi_{1L}, \\ \psi_{2R} \to L\psi_{2R}, \quad \psi_{2L} \to R\psi_{2L},\end{aligned} \tag{13}$$

where R is an element of the $SU(2)_R$ chiral symmetry group and L is an element of the $SU(2)_L$ chiral symmetry group. Here m_0 represents the chiral-invariant mass.

The mesonic part of the Lagrangian reads

$$\begin{aligned}\mathcal{L}_M = {} & \frac{1}{2}\partial_\mu\sigma\partial^\mu\sigma + \frac{1}{2}\partial_\mu\vec{\pi}\cdot\partial^\mu\vec{\pi} \\ & - \frac{1}{4}\Omega_{\mu\nu}\Omega^{\mu\nu} - \frac{1}{4}\vec{R}_{\mu\nu}\cdot\vec{R}^{\mu\nu} - \frac{1}{4}F_{\mu\nu}F^{\mu\nu} \\ & + \frac{1}{2}\bar{\mu}^2(\sigma^2 + \vec{\pi}^{\,2}) - \frac{\lambda}{4}(\sigma^2 + \vec{\pi}^{\,2})^2 + \frac{1}{6}\lambda_6(\sigma^2 + \vec{\pi}^{\,2})^3 \\ & + \epsilon\sigma + \frac{1}{2}m_\omega^2\omega_\mu\omega^\mu + \frac{1}{2}m_\rho^2\vec{\rho}_\mu\cdot\vec{\rho}^{\,\mu},\end{aligned} \tag{14}$$

where $\Omega_{\mu\nu}$, $\vec{R}_{\mu\nu}$, and $F_{\mu\nu}$ are in Eqs. (8)–(10).

The collective meson field $M = \sigma + i\boldsymbol{\tau}\cdot\boldsymbol{\pi}$ transforms as

$$M \to LMR^\dagger. \tag{15}$$

We note here that the pion mass m_π, σ meson mass m_σ, and pion-decay constant f_π can be related to the parameters λ, $\bar{\mu}^2$, and λ_6 in vacuum:

$$\begin{aligned}m_\pi^2 &= \lambda\sigma_0^2 - \bar{\mu}^2 - \lambda_6\sigma_0^4, \\ m_\sigma^2 &= 3\lambda\sigma_0^2 - \bar{\mu}^2 - 5\lambda_6\sigma_0^4, \\ f_\pi &= \sigma_0,\end{aligned} \tag{16}$$

with $m_\pi = 138$ MeV, $f_\pi = 93$ MeV, and $\sigma_0 = f_\pi$ being the vacuum expectation value of the σ field. The mass of the σ meson in this work is treated as a free parameter, while the masses of ω and ρ meson are set to $m_\omega = 783$ MeV and $m_\rho = 776$ MeV.

We now make the mean-field approximation by replacing the σ, ω, and the ρ field by their mean fields $\sigma \to \bar{\sigma}$, $\omega_\mu \to \delta_{\mu0}\bar{\omega}_0$, and $\rho_{i\mu} \to \delta_{i3}\delta_{\mu0}\bar{\rho}_0^3$. The equations of motion (EoM) for the stationary mean fields $\tilde{\sigma} = \bar{\sigma} - \sigma_0$, $\bar{\omega}$, $\bar{\rho}$, and $\bar{A}_0$ read

$$\begin{aligned}\big(-\vec{\nabla}^2 + m_\sigma^2\big)\tilde{\sigma}(\vec{x}) = {} & -\bar{N}(\vec{x})N(\vec{x})\left.\frac{\partial m_N(\tilde{\sigma})}{\partial\tilde{\sigma}}\right|_{\tilde{\sigma}=\tilde{\sigma}(\vec{x})} \\ & + \big(-3f_\pi\lambda + 10f_\pi^3\lambda_6\big)\tilde{\sigma}(\vec{x})^2 \\ & + \big(-\lambda + 10f_\pi^2\lambda_6\big)\tilde{\sigma}(\vec{x})^3 \\ & + 5f_\pi\lambda_6\tilde{\sigma}(\vec{x})^4 + \lambda_6\tilde{\sigma}(\vec{x})^5,\end{aligned} \tag{17}$$

$$\Big(-\vec{\nabla}^2 + m_\omega^2\Big)\bar{\omega}(\vec{x}) = g_{\omega NN}N^\dagger(\vec{x})N(\vec{x}), \tag{18}$$

$$\big(-\vec{\nabla}^2 + m_\rho^2\big)\bar{\rho}(\vec{x}) = g_{\rho NN}N^\dagger(\vec{x})\tau_3 N(\vec{x}), \tag{19}$$

$$-\vec{\nabla}^2\bar{A}_0(\vec{x}) = eN^\dagger(\vec{x})\frac{1-\tau_3}{2}N(\vec{x}). \tag{20}$$

Currently, only the time component of ω, ρ, and A are included and the effect of the Laplacian term is included only for the electromagnetic potential A_0. The mass eigenstates are obtained by diagonalizing the mass matrix:

$$m_\pm = \tfrac{1}{2}\Big(\sqrt{(g_1+g_2)^2\bar{\sigma}^2 + 4m_0^2} \mp (g_1 - g_2)\bar{\sigma}\Big). \tag{21}$$

The nucleon mass is $m_N = m_+$ since they have positive parity. Its negative-parity partner has m_-. Note that $\bar{\sigma} = \tilde{\sigma} + \sigma_0$ is the in-medium average that depends on the environment.

By using the nucleon mass, meson masses, and pion-decay constant, one can determine meson coupling constants g_1, g_2, g_ω, g_ρ and parameters λ, $\bar{\mu}^2$, and λ_6. The nuclear matter properties used to fix these parameters are given by

$$\begin{aligned}\frac{E}{A} - m_N = -16\ \text{MeV}, \quad n_0 = 0.16\ \text{fm}^{-3}, \\ K = 240 \pm 40\ \text{MeV}, \quad E_{\text{sym}} = 31\ \text{MeV}.\end{aligned} \tag{22}$$

Note that the compressibility K has a relatively large uncertainty compared with other nuclear matter properties. Hence, we consider two different values of the compressibility as inputs, $K = 215$ and 240 MeV. In Table IV, we summarize the parameter sets used in this work. These parameter sets are taken from Ref. [32] except for the sets with $m_0 = 500$ with which binding-energy and charge-radius calculations do not converge. In the nuclear structure studies [32], chiral-invariant mass $m_0 = 700$ MeV is preferred.

TABLE IV. Parameter sets used in this work with different compressibility: $K = 215$ and $K = 240$ MeV. m_0 and m_σ are in MeV. The parameter sets which are fixed to fit nuclear matter properties for given compressibility K and m_0 [32].

	$K = 215$ MeV				$K = 240$ MeV			
m_0	600	700	800	900	600	700	800	900
g_1	14.836	14.1708	13.3493	12.3293	14.836	14.1708	13.3493	12.3293
g_2	8.42735	7.76222	6.94073	5.92073	8.42735	7.76222	6.94073	5.92073
g_ω	8.90217	7.05508	5.47079	3.38862	9.13193	7.30465	5.65978	3.52185
g_ρ	3.97462	4.07986	4.15669	4.22091	3.92698	4.06502	4.14894	4.21785
$\bar{\mu}^2/f_\pi^2$	23.3772	20.9799	13.3463	2.50198	21.8212	18.8421	11.6928	1.5374
λ	42.3692	38.921	26.1283	6.673	39.3674	34.5841	22.5779	4.38835
$\lambda_6 f_\pi^2$	16.7901	15.7393	10.5802	1.96915	15.3444	13.5401	8.68327	0.649073
m_σ	413.612	384.428	324.007	257.583	411.299	385.805	330.44	269.255

V. APPLICATION OF EXTENDED PARITY DOUBLET MODEL TO HEAVY-ION COLLISIONS

As an application of EPDM to heavy-ion collisions, we consider ^{197}Au + ^{197}Au collisions with our new transport code DJBUU. In this work, we focus on the time evolution of the effective masses and anisotropic collective flow.

A. Time evolution of effective masses

The energies required to produce new particles in a dense medium can be obtained from the dispersion relation:

$$E_n = \sqrt{m_N{}^2 + \mathbf{k}^2} + g_\omega \bar{\omega} - g_\rho \bar{\rho},$$
$$E_p = \sqrt{m_N{}^2 + \mathbf{k}^2} + g_\omega \bar{\omega} + g_\rho \bar{\rho}, \tag{23}$$

where E_n and E_p are the energies of a neutron and a proton and m_N is the density-dependent nucleon mass m_+ defined in Eq. (21). As in Ref. [29], we define the effective nucleon masses as energies at $\mathbf{k} = 0$ from the dispersion relation:

$$m_n^{(\mathrm{eff})} = m_N + g_\omega \bar{\omega} - g_\rho \bar{\rho},$$
$$m_p^{(\mathrm{eff})} = m_N + g_\omega \bar{\omega} + g_\rho \bar{\rho}. \tag{24}$$

As in other mean-field models, there are significant effective-mass splitting between protons and neutrons as the isospin density increases.

Figure 9 summarizes the time evolution of effective masses at the central part in ^{197}Au + ^{197}Au head-on collision at 400A MeV. From Eq. (24), one can see that the exchange of isospin-dependent ρ mesons causes mass splitting between protons and neutrons.

The maximum value of the splitting increases as m_0 increases for both compressibilities. But the maximum values of the splitting barely depend on the compressibility for a given m_0. Maximum density increases as m_0 increases and lies in the range $1.44 < \rho_{\max}/\rho_0 < 2.0$. The 1σ statistical uncertainties in our calculations are rather small and thus not shown in the figure. For instance, with $m_0 = 700$ MeV and $K = 240$ MeV, the maximum density is calculated to be 0.2523 ± 0.0032 fm^{-3}. One clear trend is that the maximum density increases as the chiral-invariant mass m_0 increases. This behavior can be explained in terms of the behavior of the σ field and the ω field. In Fig. 10, the expectation values of σ and ω meson fields are summarized. One can see that the ω mean field decreases faster with increasing m_0 than does the σ mean field. Because ω provides repulsion and σ provides attraction, a larger value of m_0 naturally results in a larger value of the nucleon density.

If one can measure or estimate the maximum densities in HICs, the value of the chiral-invariant mass m_0 could be narrowed down.

B. Anisotropic collective flow

The heavy-ion collisions with a finite impact parameter develop an anisotropic collective flow in momentum distribution. Since the flow depends on the mean fields, collisions, blocking, etc., it can provide valuable information on a dense medium. In general, the flow can be quantified in terms of the Fourier expansion of the momentum density in the azimuthal angle ϕ [39]:

$$\frac{dN}{dyd^2p_t} \propto 1 + 2\sum_{n=1}^{\infty} v_n(y, p_t)\cos[n(\phi - \psi_n)], \tag{25}$$

where ψ_n is the event plane angle for the nth harmonics. The first two flow coefficients v_1 and v_2 are often referred to as the "direct" and "elliptic" flows, respectively. The flow coefficients $v_n(y, p_t)$ are the functions of rapidity y and transverse momentum $p_t = (p_x^2 + p_y^2)^{1/2}$. Here we focus on the directed flow defined as $v_1 = \langle p_x/p_t \rangle$ for the particles with positive rapidity. Note that one can always set $\psi_1 = 0$ by reorienting the system.

The directed flow v_1 of protons as a function of reduced rapidity is shown in Fig. 11. The results shown are for the ^{197}Au + ^{197}Au collisions at $E_{\mathrm{beam}} = 400A$ MeV. To match the FOPI cuts [41,42], we define two scaled parameters. The scaled impact parameter is defined as $b_0 = b/b_{\max}$ where $b_{\max} = 1.15 \times (A_P^{1/3} + A_T^{1/3})$. The scaled transverse velocity is defined as $u_{t0} = u_t/u_p$ where u_t is the transverse component of the four-velocity of a particle and u_p is the beam direction component of the four-velocity of the beam. The cuts we impose are $0.25 < b_0 < 0.45$ and $u_{t0} > 0.4$.

In Fig. 11, one can see that the proton directed flows with $m_0 = 600$, 700, and 800 MeV are all roughly consistent with experiments and there is not much sensitivity to the compressibility. One may say that the highest chiral-invariant mass tested, $m_0 = 900$ MeV, is disfavored because it deviates from

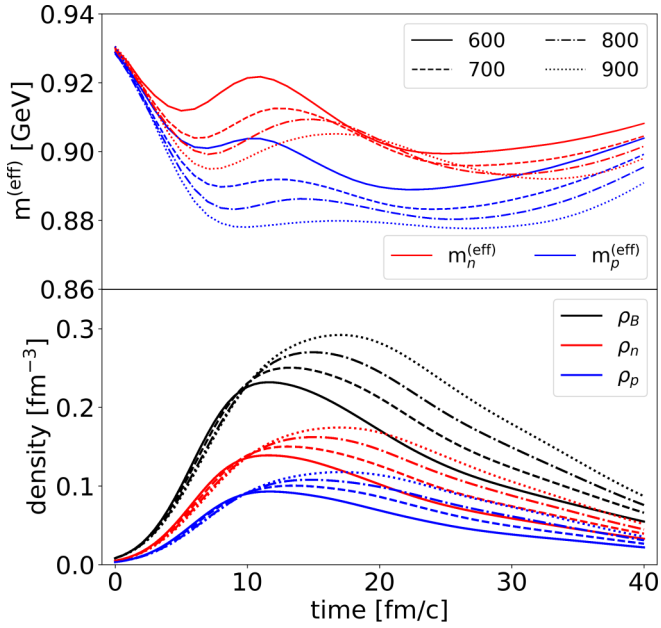

(a) $K = 215$ MeV

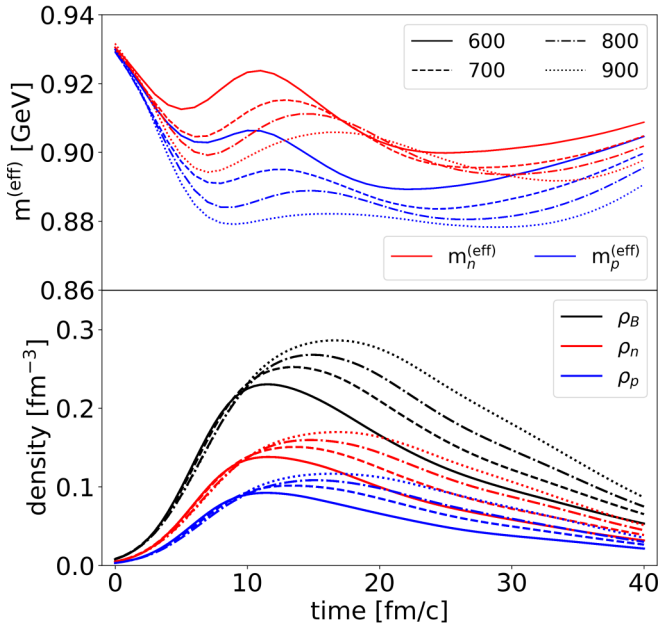

(b) $K = 240$ MeV

FIG. 9. Time evolution of neutron and proton effective masses and densities at the center in ^{197}Au + ^{197}Au head-on collisions with $E_{\rm beam} = 400A$ MeV and different compressibilities $K = 215$ and 240 MeV. The red color indicates physical quantities of neutrons while blue is for protons. The black color represents baryon (neutron + proton) quantities. The solid, dashed, dash-dotted, and dotted lines are for $m_0 = 600$, 700, 800, and 900 MeV, respectively.

the data at higher rapidities. This can be again explained by the weaker ω field which would not provide enough repulsion. However, the deviation is not significant enough for a firm conclusion.

In Fig. 12, the nucleon rapidity distributions of two nuclei at the initial time (dashed line) and the final time (solid

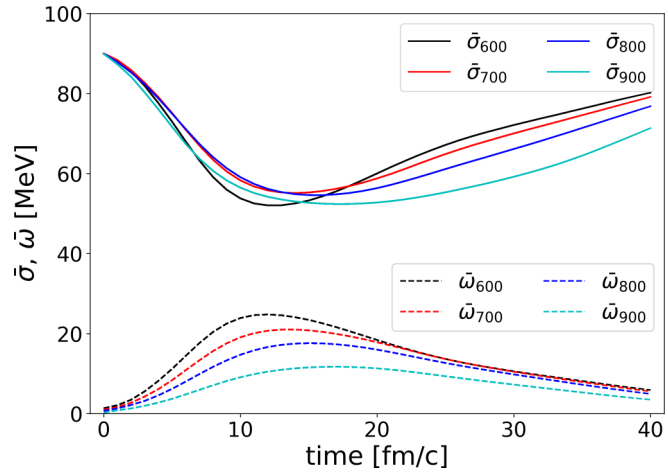

FIG. 10. Time evolution of $\bar{\sigma}$ and $\bar{\omega}$ for ^{197}Au + ^{197}Au central collision at the center position of the center-of-mass frame.

lines) for four different chiral-invariant masses are plotted. In this figure, only $K = 215$ MeV is shown. Setting $K = 240$ yields similar results. The rapidity distribution along the beam axis reflects the nucleon stopping effects in HICs. The initial distributions have peaks at $y/y_{\rm beam} = \pm 1$ because particles are distributed around the beam rapidities at the initial time. The stopping is largely insensitive to the value of the chiral-invariant mass.

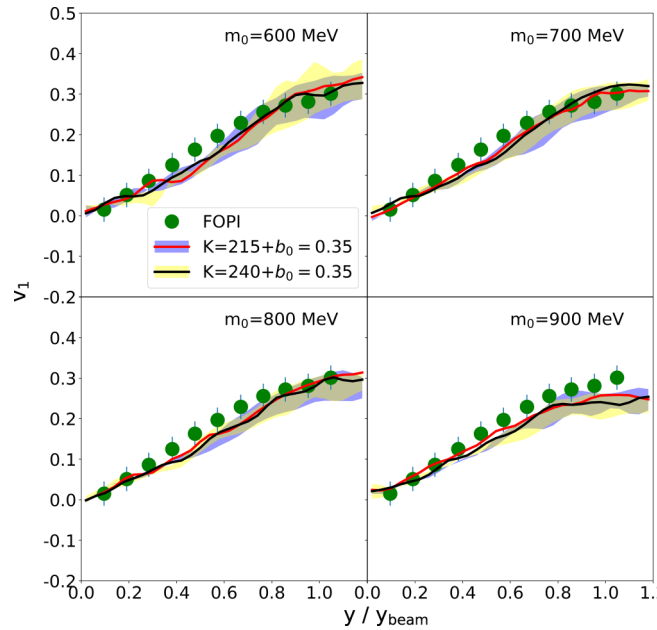

FIG. 11. Proton directed flow as a function of reduced rapidity for ^{197}Au + ^{197}Au collisions with $0.25 < b_0 < 0.45$ at $E_{\rm beam} = 400A$ MeV. Two values of compressibility, $K = 215$ MeV (purple shaded area) and $K = 240$ MeV (yellow shaded are), are considered. Upper and lower limits of each shaded area correspond to the upper and lower limits of the impact parameter b_0, and the solid line corresponds to the mean value $b_0 = 0.35$. FOPI data are taken from Ref. [40].

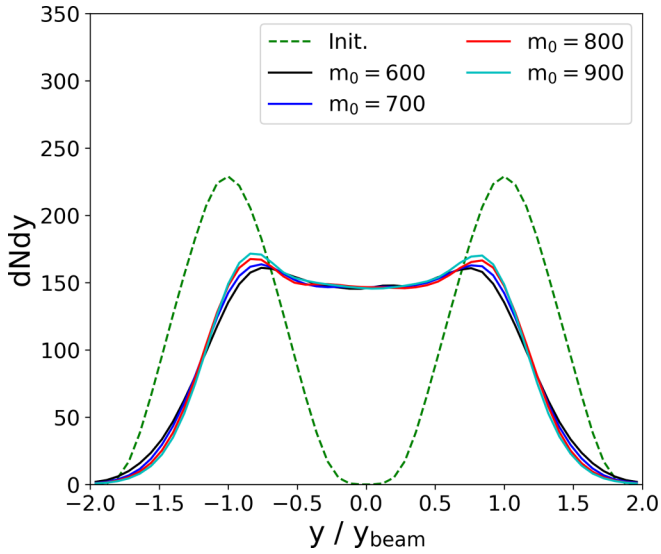

FIG. 12. Nucleon rapidity distributions at the beam energy of 400A MeV at $b_0 = 0.35$ fm with $K = 215$ MeV.

VI. SUMMARY AND CONCLUSIONS

In this work, we have studied low-energy heavy-ion collisions and infinite dense matter by using DJBUU which is a new transport code of relativistic Boltzmann-Uehling-Uhlenbeck type. To test the validity of DJBUU, we compared our results with those reported in the Transport Code Comparison Project studies. We found that our results are consistent with the TCCP results, such as nuclei stability, time evolution of density in Au + Au collisions, Pauli blocking and collisions, rapidity distribution, and collision itself in box calculations.

After confirming the validity of DJBUU, we implemented the extended parity doublet model in DJBUU for heavy-ion collision simulations. For the time evolution of effective masses in the medium, we simulated central ^{197}Au + ^{197}Au collisions at $E_{\rm beam} = 400A$ MeV for four different values of m_0. In general, the mass splitting between protons and neutrons are found to increase as the chiral-invariant mass increases. We also found that the results are not so sensitive to the compressibility. The proton directed flow and rapidity distribution have been studied and compared with the experimental result of FOPI. We found that $m_0 = 600$, 700, 800, and 900 MeV give similar results as far as directed flow is concerned, even though there are some deviations at the large-rapidity region for $m_0 = 900$ MeV.

In the future, other nuclear models, such as KIDS [43], will be tested with DJBUU, and our numerical calculations will be compared with the results from future rare-isotope experiments within a few hundred A MeV.

ACKNOWLEDGMENTS

M.K. and C.-H.L. were supported by National Research Foundation of Korea (NRF) grants funded by the Korean government (Ministry of Science and ICT and Ministry of Education) (No. 2016R1A5A1013277 and No. 2018R1D1A1B07048599). S.J. was supported in part by the Natural Sciences and Engineering Research Council of Canada. Y.-M.K. was supported by NRF Grants (No. 2016R1A5A1013277 and No. 2019R1C1C1010571). Y.K. was supported by the Rare Isotope Science Project of Institute for Basic Science funded by Ministry of Science and ICT and NRF Grant (No. 2013M7A1A1075764). Y.K. acknowledges useful discussions with Masayasu Harada.

[1] T. Motobayashi, EPJ Web Conf. **66**, 01013 (2014).
[2] G. F. Bertsch, H. Kruse and S. Das Gupta, Phys. Rev. C **29**, 673 (1984); **33**, 1107(E) (1986).
[3] H. Kruse, B. V. Jacak, J. J. Molitoris, G. D. Westfall, and H. Stocker, Phys. Rev. C **31**, 1770 (1985).
[4] J. Aichelin, Phys. Rev. C **33**, 537 (1986).
[5] E. E. Kolomeitsev, C. Hartnack, H. W. Barz, M. Bleicher *et al.*, J. Phys. G **31**, S741 (2005).
[6] J. Xu, L. W. Chen, M. Y. B. Tsang, H. Wolter, Y. X. Zhang, J. Aichelin, M. Colonna, D. Cozma, P. Danielewicz, Z. Q. Feng, A. LeFevre, T. Gaitanos, C. Hartnack, K. Kim, Y. Kim, C. M. Ko, B. A. Li, Q. F. Li, Z. X. Li, P. Napolitani *et al.*, Phys. Rev. C **93**, 044609 (2016).
[7] Y. X. Zhang, Y. J. Wang, M. Colonna, P. Danielewicz, A. Ono, M. B. Tsang *et al.*, Phys. Rev. C **97**, 034625 (2018).
[8] A. Ono, J. Xu, M. Colonna, P. Danielewicz, C. M. Ko, M. B. Tsang *et al.*, Phys. Rev. C **100**, 044617 (2019).
[9] T. Gaitanos, A. B. Larionov, H. Lenske, and U. Mosel, Phys. Rev. C **81**, 054316 (2010).
[10] A. B. Larionov, T. Gaitanos, and U. Mosel, Phys. Rev. C **85**, 024614 (2012).
[11] O. Buss *et al.*, Phys. Rep. **512**, 1 (2012).
[12] B. A. Li, L. W. Chen, and C. M. Ko, Phys. Rep. **464**, 113 (2008).
[13] B. A. Li, C. M. Ko, and Z. Ren, Phys. Rev. Lett. **78**, 1644 (1997).
[14] B. A. Li, C. M. Ko, and W. Bauer, Int. J. Mod. Phys. E **7**, 147 (1998).
[15] L. W. Chen, C. M. Ko, B. A. Li, C. Xu, and J. Xu, Eur. Phys. J. A **50**, 29 (2014).
[16] C. Fuchs and H. H. Wolter, Nucl. Phys. A **589**, 732 (1995).
[17] T. Gaitanos, M. Di Toro, S. Typel, V. Baran, C. Fuchs, V. Greco, and H. H. Wolter, Nucl. Phys. A **732**, 24 (2004).
[18] G. Ferini, T. Gaitanos, M. Colonna, M. Di Toro and H. H. Wolter, Phys. Rev. Lett. **97**, 202301 (2006).
[19] C. De Tar and T. Kunihiro, Phys. Rev. D **39**, 2805 (1989).
[20] D. Jido, M. Oka, and A. Hosaka, Prog. Theor. Phys. **106**, 873 (2001).
[21] T. Hatsuda and M. Prakash, Phys. Lett. B **224**, 11 (1989).
[22] D. Zschiesche, L. Tolos, J. Schaffner-Bielich, and R. D. Pisarski, Phys. Rev. C **75**, 055202 (2007).
[23] V. Dexheimer, S. Schramm, and D. Zschiesche, Phys. Rev. C **77**, 025803 (2008).
[24] C. Sasaki and I. Mishustin, Phys. Rev. C **82**, 035204 (2010).
[25] S. Gallas, F. Giacosa, and G. Pagliara, Nucl. Phys. A **872**, 13 (2011).

[26] J. Steinheimer, S. Schramm, and H. Stocker, Phys. Rev. C **84**, 045208 (2011).
[27] S. Benic, I. Mishustin, and C. Sasaki, Phys. Rev. D **91**, 125034 (2015).
[28] Y. Motohiro, Y. Kim, and M. Harada, Phys. Rev. C **92**, 025201 (2015); **95**, 059903(E) (2017).
[29] Y. Takeda, Y. Kim, and M. Harada, Phys. Rev. C **97**, 065202 (2018).
[30] Y. Takeda, H. Abuki, and M. Harada, Phys. Rev. D **97**, 094032 (2018).
[31] M. Marczenko, D. Blaschke, K. Redlich, and C. Sasaki, Phys. Rev. D **98**, 103021 (2018).
[32] I. J. Shin, W-G. Paeng, M. Harada, and Y. Kim, arXiv:1805.03402.
[33] B. Liu, V. Greco, V. Baran, M. Colonna and M. Di Toro, Phys. Rev. C **65**, 045201 (2002).
[34] C. Y. Wong, Phys. Rev. C **25**, 1460 (1982).
[35] M. Kim, C.-H. Lee, Y. Kim, and S. Jeon, Sae Mulli **66**, 1563 (2016).
[36] M. Colonna (private communication).
[37] X. Jin, Y. Zhuo, and X. Zhang, Nucl. Phys. A **506**, 655 (1990).
[38] Y. Abe, S. Ayik, P. G. Reinhard, and E. Suraud, Phys. Rep. **275**, 49 (1996).
[39] J. Y. Ollitrault, Phys. Rev. D **46**, 229 (1992).
[40] W. J. Xie and F. S. Zhang, Phys. Lett. B **735**, 250 (2014).
[41] W. Reisdorf *et al.* (FOPI Collaboration), Nucl. Phys. A **781**, 459 (2007).
[42] W. Reisdorf *et al.* (FOPI Collaboration), Nucl. Phys. A **876**, 1 (2012).
[43] P. Papakonstantinou, T. S. Park, Y. Lim, and C. H. Hyun, Phys. Rev. C **97**, 014312 (2018).